Available online at www.sciencedirect.com
ScienceDirect
Coordination Chemistry Reviews 252 (2008) 1497–1513
COORDINATION CHEMISTRY REVIEWS
www.elsevier.com/locate/ccr

Review

Density-functional molecular dynamics studies of biologically relevant iron and cobalt complexes with macrocyclic ligands

Ivan Degtyarenko [a], Xevi Biarnés [b], Risto M. Nieminen [a], Carme Rovira [b,c,*]

[a] *Laboratory of Physics, Helsinki University of Technology, P.O.B. 1100, FIN-02015 Hut, Finland*
[b] *Centre de Recerca en Química Teòrica, Parc Científic de Barcelona, Josep Samitier 1-5, 08028 Barcelona, Spain*
[c] *Institució Catalana de Recerca i Estudis Avançats (ICREA), Passeig Lluís Companys 23, 08018 Barcelona, Spain*

Received 16 June 2007; accepted 22 October 2007
Available online 19 December 2007

Contents

Abstract

In this manuscript we review our recent work on the structure and dynamics of iron and cobalt complexes with macrocyclic ligands using *ab initio* molecular dynamics (AIMD). AIMD techniques are used to analyze the short time scale dynamics of these complexes, helping to understand the results obtained by experimental methods with larger time resolution. Firstly, the case of the iron–oxygen bond in myoglobin (Mb) and hemoglobin (Hb), as well as its cobalt analogues, will be discussed. Secondly, we will focus on the B_{12} coenzyme and its organocobaloxime derivatives. The simulations grasp the role played by temperature on the dynamics of ligands (the FeO_2 and CoO_2 moieties in heme models and the bridging OH···O protons in organocobaloxime crystals), clarifying problems related to average structures and underscoring the need to perform dynamical simulations.

Keywords: *Ab initio* molecular dynamics; Car–Parrinello method; Heme models; Adenosylcobalamin; Methylcobalamin; Organocobalt complexes

1. Introduction

Cobalt and iron are present in a variety of biological structures in which the metal atom is part of a macrocycle such as porphyrin and corrin (Fig. 1). They have also received considerable attention for some time, owing to their spectral signatures as well as their rich ligand substitution and redox chemistry [1]. Two of the most studied biological systems based on iron and cobalt macrocycles are hemeproteins and B_{12}-dependent enzymes.

* Corresponding author at: Centre de Recerca en Química Teòrica, Parc Científic de Barcelona, Josep Samitier 1-5, 08028 Barcelona, Spain.
Tel.: +34 934037112; fax: +34 934037225.
E-mail address: crovira@pcb.ub.es (C. Rovira).

0010-8545/$ – see front matter © 2007 Elsevier B.V. All rights reserved.
doi:10.1016/j.ccr.2007.10.022

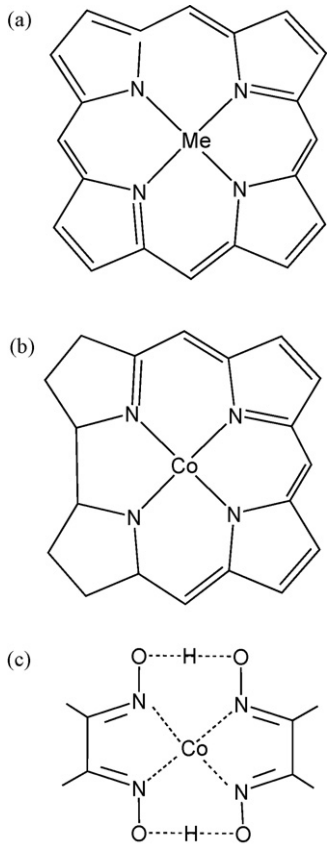

Fig. 1. (a) Me-porphyrin (Me = iron, cobalt), (b) cobalt-corrin and (c) cobalt-bisdimethylglyoxime.

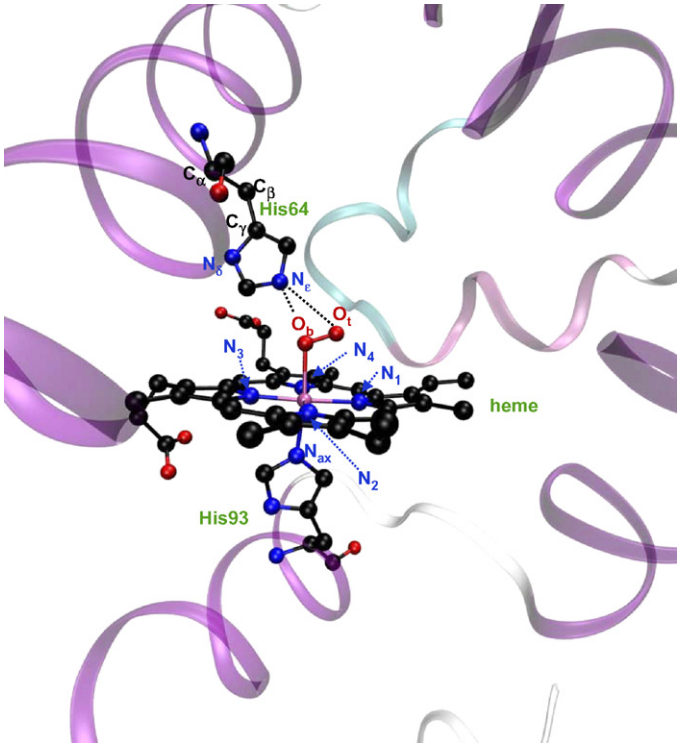

Fig. 2. Structure of $CoMbO_2$ (PDB entry 1YOI). There is a covalent bond between the heme iron and the nitrogen atom of the His93 residue (*proximal histidine*). H-atoms are not shown, dashed N_ε–$O_{(t,b)}$ lines indicate N_ε–H···$O_{(t,b)}$ hydrogen bonding interaction. Reproduced from Ref. [23], with permission of the copyright holders.

Hemeproteins play an important role in oxygen transport and storage (hemoglobin and myoglobin), catalysis of the decomposition of toxic species (catalases and peroxidases), electron transport (cytochromes) and signaling processes (guanylate cyclase), among others. The efficiency of these processes relies on the electronic properties of the versatile heme active center (Fig. 2), which dictates its reactivity and ligand-binding properties. The oxygen-carrying proteins, hemoglobin (Hb) and myoglobin (Mb), have often been used as examples of protein conformation, dynamics, and function [2]. Their structure is known nowadays with atomic resolution and the kinetics of ligand binding and recombination are studied in detail [3]. One of the major questions in the research on Hb and Mb is how the protein discriminates against the binding of endogenous ligands such as CO, i.e. the fact that the CO/O_2 ligand affinity ratio between decreases by three orders of magnitude in the protein compared to synthetic heme analogues [4]. It was believed early that steric factors (i.e. protein-induced distortion of the Fe–CO angle with respect to the linearity) were the origin of this discrimination. However, during the last years a number of investigations, mainly X-ray, kinetic, thermodynamic, spectroscopic, and theoretical techniques have challenged this interpretation (see Refs. [5–8] for recent reviews). Most authors now accept that the binding of O_2 is favored by hydrogen bonding with the distal His (His64 in Fig. 2) [9–12], as found early in neutron and X-ray diffraction measurements in MbO_2 and HbO_2 [13,14]. Crystal structures, however, give a static position of the ligand, and its dynamical motion is only known in an indirect way. For instance, the fact that the local structure of the FeO_2 fragment differs significantly among different structures is indicative of a high flexibility of the FeO_2 unit. Even if the most recent crystal structure of HbO_2 (PDB entry 2DN1, at 1.30 Å resolution) solves most of the problems affecting early structure determinations [14], it still gives two very different O–O distances for the α and β subunits (1.23 and 1.41 Å, respectively). A higher degree of rotation of the O_2 ligand around the Fe–O bond in the β subunit, compared to the α subunit, was inferred from the lower electron density at the terminal oxygen atom compared to the α unit. In other cases, the exact position of the ligand could not be given, presumably due to the free rotation of the ligand around its equilibrium position [14]. Evidence of the dynamical motion of O_2 is also provided by investigations of synthetic models such as the oxygen-picket-fence complexes [Fe(TpivPP)(*x*-MeIm)(O_2), *x* = 1,2 or 2] (Fig. 3), for which multiple conformations for the ligand are usually obtained [15,16].

The dynamics of the metal–oxygen bonds in Hb and Mb have been investigated mainly for cobalt analogues [17–19] and the results have been typically extrapolated to iron. Cobalt replacement has the important advantage that the complexes can be studied by electron paramagnetic resonance (EPR) and electron nuclear double resonance (ENDOR) due to the S = 1/2 electron configuration of Co-heme-O_2 complex, while the Fe-heme-O_2 is EPR silent [20]. EPR studies have shown that the O_2 lig-

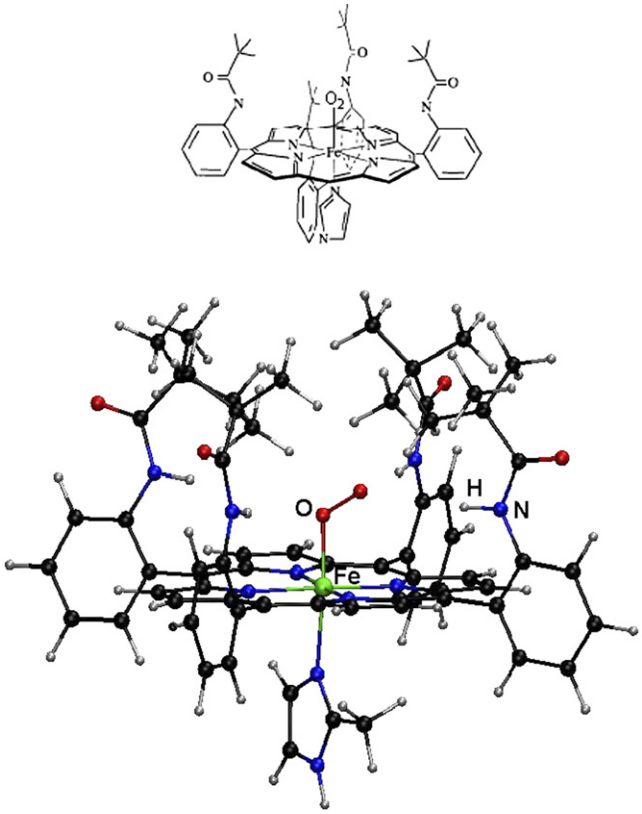

Fig. 3. The $MeT_{piv}PP(2\text{-}meIm)O_2$ molecule (Me = Fe, Co). (a) Molecular structure. (b) Optimized structure.

and undergoes a fast rotational motion around the Co–O_2 bond in models [21], HbO_2 and MbO_2, providing a different view from that obtained in X-ray structures [22]. Based on these studies, the fourfold disorder found in the crystal structures of oxyheme models (Fig. 3) and hemeproteins [14,15] has been interpreted as a dynamical disorder of the ligand along four equivalent sites. These issues can also be investigated by theoretical techniques. As the calculations can be performed on cobalt and iron analogues under the same conditions, ligand-binding properties can be directly compared [23]. Classical molecular dynamics techniques have been used in a number of investigations of ligand binding to myoglobin (see for instance Ref. [24]). However, the available force-fields are not able to describe neither the rotational dynamics of the ligand nor its electronic properties, thus the use of *ab initio* molecular dynamics is required.

A cobalt-based macrocycle, corrin, is the central core of vitamin B_{12} or cobalamin. The two-coenzyme forms of B_{12} are adenosylcobalamin (AdoCbl) and methylcobalamin (MeCbl), shown in Figs. 4 and 5. These molecules act as cofactors of enzymes involved in several relevant biological reactions [25–30] such as methyl transfer reactions and radical reactions involving the interchange of a functional group (e.g. alkyl fragment, –OH or $–NH_2$) and a hydrogen. AdoCbl and MeCbl are the only natural biomolecules that contain corrin [31], which is the most saturated among all tetrapyrrole molecules with two directly connected pyrroles [32]. The corrin macrocycle differs from porphyrin in having one less meso carbon atom, thus it

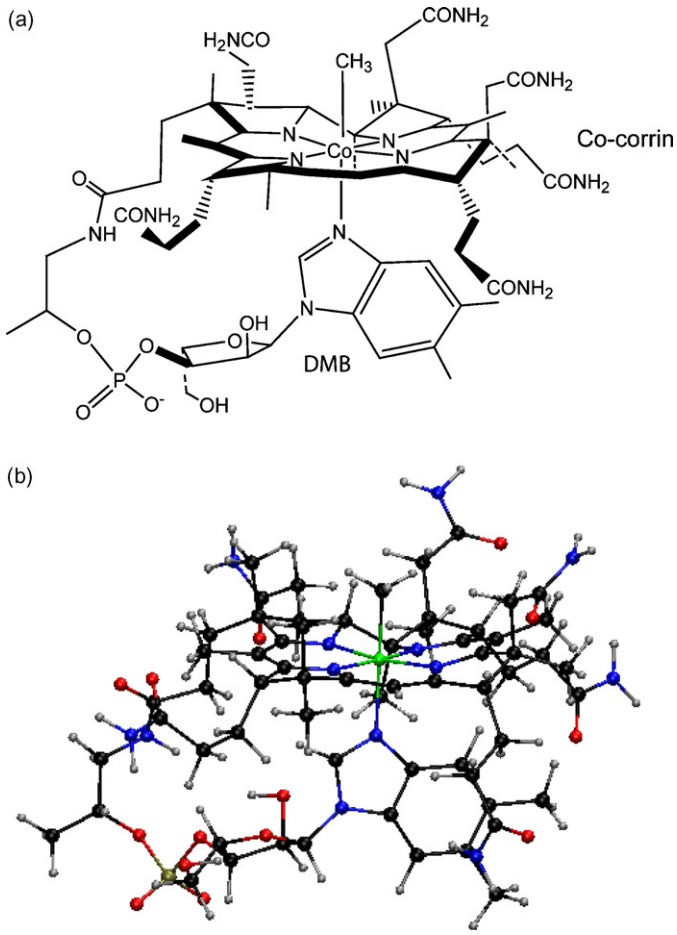

Fig. 4. The MeCbl cofactor. (a) Chemical structure. (b) Ball and stick representation of the optimized structure.

is less aromatic and also non-planar. The MeCbl and AdoCbl molecules are built from a cobalt-corrin macrocycle (Fig. 1b) with several acetamide, propanamide, and methyl substituents (Fig. 4) [30]. The central Co(III) atom is in an octahedral environment, with methyl/adenosyl and benzimidazole (BZM) in the axial positions (Fig. 4). The latter is part of a nucleotide that is connected to the corrin ring via one of the propanamide corrin substituents. In some B_{12}-dependent enzymes, the BZM is released and replaced by a histidine residue of the protein [33].

The search for functional analogues of the B_{12} coenzyme has led to an important area of research based on the synthesis of similar macrocyclic ligands. Organocobaloximes have been widely studied as models for the vitamin B_{12} coenzyme [34,35]. Most of them have the formula $Co(dmgH)_2(L)R$ where dmgH is the monoanion of dimethylglyoxime, L is an axial base and R is an organoligand. A large number of cobaloximes with different R and L ligands have been reported [34], with R being CH_3, CCl=CHCl, Cl or H_2O, among others. The axial base (L) is often a nitrogen-coordinated molecule such as pyridine or imidazole.

The two equatorial dimethylglyoxime ligands are commonly present as monoanionic (dmgH) and the corresponding configuration is denoted as $(dmgH)_2$ (Fig. 1c) Nevertheless, a $dmg/dmgH_2$ configuration, in which both protons are attached to one of the two dimethylglyoxime ligands ($dmgH_2$), while the other ligand remains deprotonated (dmg^{2-}), is occasion-

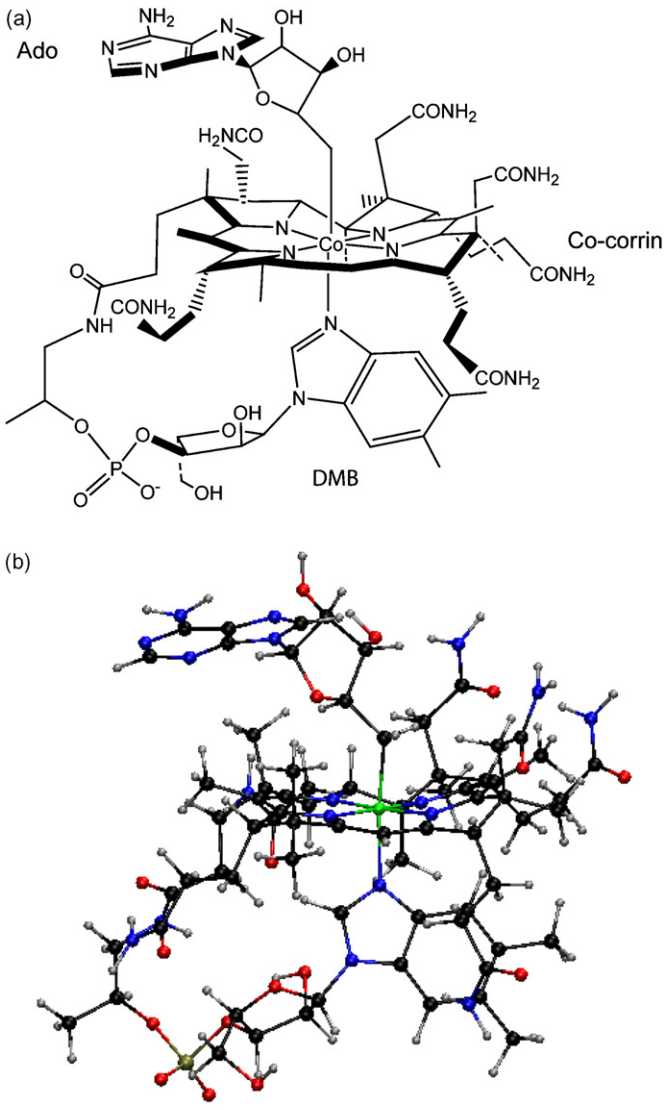

Fig. 5. The AdoCbl cofactor. (a) Chemical structure. (b) Ball and stick representation of the optimized structure.

ally found [34] (see Fig. 1c). This has been attributed to the involvement of additional interactions such as strong hydrogen bonds [36,37], or localized π–π interactions between the equatorial ligand and phenyl groups of the axial ligand [38]. From an experimental point of view, the protonation state of the dimethylglyoxime ligands (dmg^{2-}, $dmgH^{-}$ or $dmgH_2$) can be identified by a slight lengthening of the Co–N and N–O distances in the $dmgH_2$ unit with respect to those of the dmg unit [34]. For instance, in the case of $Co(NO_2)(H_2O)(dmg)(dmgH_2)$ [37] the N–O distances associated with the dianionic ligand (dmg) are 0.06 Å shorter than the ones associated to the neutral ligand ($dmgH_2$). In the case of Co(4-CA)(Cl)(dmg)($dmgH_2$) (CA = chloroaniline) the Co–N distances corresponding to the unprotonated NO unit are 0.03 Å shorter than the ones of the protonated one [38]. However, as the changes in the Co–N and N–O distances are very small and the positions of the hydrogen atoms are generally not available, the assignment from the structural data alone is often not possible. This is the case, for instance, of the cobaloxime complex [Co(CCl=CHCl)$(dmgH)_2$(py)]. $CHCl_3$ [39], for which all Co–N and N–O distances are equivalent in the X-ray structure. This complex has recently received considerable attention because of the role of chlorovinylcobalt complexes in the reaction cycle of dehalogenases [40–42].

In this manuscript we review our recent work on the structure and dynamics of iron and cobalt complexes with macrocyclic ligands using *ab initio* molecular dynamics. In Section 3 we summarize our recent studies on the structure and ligand dynamics of myoglobin mimetic models, additionally we report results of picket-fence models simulations. In Section 4 we review the work on the structure and dynamics of B_{12} models, in particular, we show how the protonation state of the ligands can be elucidated by means of *ab initio* molecular dynamics simulations.

2. Computational details

All calculations reported here were performed using density-functional theory (DFT) based molecular dynamics methods. The calculations of the B_{12} coenzyme and its organocobaloxime biomimetics were done using the CPMD code [43,44], which is based on the Car–Parrinello method [45]. The Kohn–Sham orbitals were expanded in a plane wave basis set with the kinetic energy cutoff of 70 Ry. We employed norm-conserving scalar relativistic pseudopotentials [46], and the non-linear core-correction [47] was applied to improve the transferability of the Co pseudopotential. The calculations were made using the generalized gradient-corrected approximation (GGA) of the spin-dependent density-functional theory (DFT-LSD), following the prescription of Becke and Perdew (BP) [48,49]. The quantum-mechanical (QM) system was enclosed in an isolated supercell of size 15,341 Å × 21,160 Å × 20,102 Å/22,483 Å × 18,780 Å × 18,515 Å (organocobaloximes), 22 Å × 18 Å × 17 Å (MeCbl) and 20 Å × 20 Å × 20 Å (AdoCbl). Structural optimizations were performed by means of molecular dynamics with annealing of the atomic velocities, until the maximum component of the nuclear gradient was lower than 10^{-5} a.u. Periodic calculations were done taking into account only the Γ point of the Brillouin zone. Molecular dynamics simulations used a time step of 0.12 fs and the fictitious mass of the electrons was set at 700 a.u. The deuterium mass was used for hydrogen, which allows a longer simulation step to be used. The total length of the simulations was 5–6 ps for each cobaloxime structure.

The longer simulations of heme models were done using the SIESTA program [50,51], which is based on Born–Oppenheimer molecular dynamics (BOMD) and a numerical atomic orbitals in the DFT approach. We used the GGA approximation and the exchange-correlation energy functional of Perdew, Burke, and Ernzerhof (PBE) [52]. Only the valence electrons were considered in the calculation, with the core being replaced by norm-conserving scalar relativistic pseudopotentials [46]. We used a split-valence double-ζ basis set including polarization orbitals for all atoms, as obtained with an energy shift of 50 meV [53]. The integrals of the self-consistent terms of the Kohn–Sham Hamiltonian were obtained with the help of a regular real space grid in which the electron density is projected. The grid spacing was determined by the maximum kinetic energy

of the plane waves that can be represented in that grid. In the present work, we used a cutoff of 150 Ry, which yields a spacing between the grid points of around 0.13 Å. We checked that the results are well converged with respect to the real space grid, and the range of the atomic orbitals. For the small $FeP(Im)O_2$ model, the results of the simulation were found to be very similar to those obtained in shorter simulations using CPMD [54,23]. The iron-containing models were computed as a singlet state (S = 0) while cobalt analogues were computed in the doublet spin state ($S = 1/2$).

3. Structure and dynamics of heme models

3.1. $MeP(Im)O_2$ (Me = Fe, Co)

The simplest models for the active site of Hb and Mb are those containing only the groups that are covalently attached to the metal center. The heme group is replaced by an iron-porphyrin (Fig. 1a) and the distal histidine (His93) (Fig. 2) is replaced by an imidazole ring. The equilibrium structures and electronic properties of iron heme models (or very similar) have been analyzed by several groups using DFT [7–9,23,54–63]. These studies have shown that such heme models reproduce the main structural properties of the active site. It was shown that inclusion of the imidazole is necessary to avoid the displacement of the iron out of the porphyrin plane [55], towards the diatomic ligand and that the heme substituents do not affect to the metal–ligand structure and binding energies [63].

Comparison between iron and cobalt heme models is provided in a recent work [23]. The optimized structures of $MeP(Im)O_2$ models (Me = Fe, Co) show that the main structural parameters (Table 1) are within the range of values reported in X-ray studies of $FeMbO_2$ [11] and $CoMbO_2$ [22]. The largest discrepancy corresponds to the Co–O distance (1.94 Å), which is 4% shorter than the experimental value (2.03 Å). On the other hand, the optimum Co–O–O angle (118°) is outside the range of values given by the X-ray structure (109 ± 5°). However, EPR measurements in $CoMbO_2$ predict a larger angle (120°) [64], which is much closer to the computed values. Instead, both the Fe–O distance (1.78 Å) and the Fe–O–O angle are in good agreement with the experiment (1.81 Å and 122°, respectively).

The main differences between iron and cobalt complexes concern the local structure of the MeO_2 fragment. The iron complex shows a shorter bond distance and a larger angle (Fe–O = 1.78 Å, <Fe–O–O = 121°) than the cobalt analogue (Co–O = 1.94 Å and <Co–O–O = 118°). Thus, there is a 0.06 Å increase in the metal–oxygen bond and a 3° decrease in the metal–oxygen angle upon changing iron for cobalt. The same trends are observed experimentally, although the differences are larger (0.22 Å and 13°, respectively) due to the above-mentioned discrepancies between the computed and experimental structures of the CoO_2 fragment.

The orientation of the O_2 molecule with respect to the porphyrin plane can be defined by the N_1–Me–O_b–O_t dihedral angle (ϕ in Fig. 6). This angle is ≈45° when the O_2 is in a staggered orientation and ≈0° when it adopts an overlapping orientation (i.e. it overlaps one Fe–N bond). Both cobalt and iron models exhibit a staggered orientation (ϕ = 46°–50° for $CoP(Im)O_2$ and ϕ = 45° for $FeP(Im)O_2$, according to Table 1), similar to heme models such as the picket-fence porphyrin [15,16,63] as well as previous DFT calculations for iron-heme models [9,55,56,58]. The staggered orientation is favored from steric and electronic points of view. On one hand, it avoids the steric repulsion between the

Table 1
Optimized structures of the heme models (Me = Fe, Co)

Model	Me–O_b	<Me–O_b–O_t	O_b–O_t	Me–N_{ax}	Me–N_{porph}	ϕ[a]
$FeP(Im)O_2$	1.78	121	1.28	2.08	2.01–2.04	45.5
	1.78	121.4	1.28	2.12	2.01–2.04	45.4
$FeP(Im)O_2\cdots$His	1.77 (a)	118.8 (a)	1.30 (a)	2.12 (a)	2.01–2.04 (a)	40.7
	1.77 (b)	118.9 (b)	1.30 (b)	2.11 (b)	2.01–2.04 (b)	38.8
$FeP(Im)O_2\cdots$His *free*[b]	1.77	119.8	1.3	2.11	2.01–2.04	40.7
$FeT_{piv}PP(2\text{-meIm})O_2$	1.78	121.1	1.29	2.18	2.01–2.04	47.6
exp $[FeT_{piv}PP(2\text{-meIm})O_2]$[c]	1.898(7)	<129(2)	>1.22(2)	2.107(4)	1.996(4)	45
exp $(FeMbO_2)$[d]	1.81	122	1.24	2.06	2.00–2.02	21.5
$CoP(Im)O_2$	1.94	117.7	1.28	2.08	2.01	49.6
	1.93	117.3	1.28	2.1	2.00–2.02	46.2
$CoP(Im)O_2\cdots$His	1.89	116.4	1.3	2.08	2.00–2.02	36.1
$CoP(Im)O_2\cdots$His *free*	1.91	116.9	1.3	2.07	2.00–2.01	45.3
$CoT_{piv}PP(2\text{-meIm})O_2$	1.92	117.8	1.29	2.14	2.00–2.01	45.9
exp $[CoT_{piv}PP(2\text{-meIm})O_2]$	–	–	–	–	–	–
exp $(CoMbO_2)$[e]	2.03	109 ± 5	1.18	2.08	1.98–2.09	−2.1

Distances are given in angstroms and angles in degrees.
[a] N_1–Me–O_b–O_t dihedral angle.
[b] The distal histidine is free to adopt any position.
[c] Ref. [16].
[d] Ref. [11].
[e] Ref. [22].

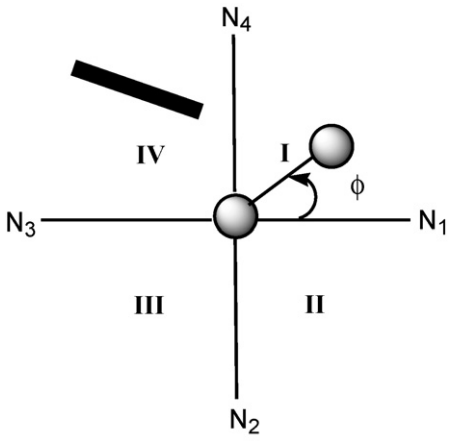

Fig. 6. Porphyrin quadrant definition. The projection of the imidazole plane of His64 on the porphyrin plane is represented with a bold line. The projection of the oxygen molecule on the porphyrin plane is shown in ball and stick. Reproduced from Ref. [23], with permission of the copyright holders.

ligand axis and the Me–N_{porph} bonds. On the other, it maximizes the interaction between the p_π orbitals of O_2 and the d_π orbitals of the metal, which are oriented along the bisectors [55]. The values of ϕ in the protein do not follow this trend, since the O_2 ligand shows an intermediate orientation between overlapping and staggered for $FeMbO_2$ ($\phi = 21^\circ$) and purely overlapping for $CoMbO_2$ ($\phi = 2^\circ$ in Table 1). This suggests that the interaction with the nearby protein residues (the distal histidine) could influence the ligand orientation.

Molecular dynamics simulations of $MeP(Im)O_2$ (M = Fe, Co) models give further insight into the conformational freedom of the ligand at room temperature. Fig. 7a shows the time evolution of the N_1–Me–O_b–O_t torsional angle (ϕ). During the first period of the simulation, the O–O axis projection on the porphyrin plane lies on the first quadrant (**I**), oscillating around the equilibrium conformation ($\phi = 45^\circ$). After ≈5 ps, the ligand jumps over the Fe–N_2 bond towards the second quadrant. Another transition takes place at ≈16 ps (back to **I**) and eventually all quadrants are sampled. This behavior provides a direct evidence for the fast rotational motion of O_2 around the Fe–O bond, as invoked to explain the fourfold disorder found in the crystal structure of synthetic heme models [15]. It also confirms that the O–O/Fe–N overlapping configuration is the transition state for the dynamic motion of O_2 between the porphyrin quadrants [79–81].

Due to the rotational motion of the ligand, the O–O axis projection on the porphyrin plane visits all porphyrin quadrants, as shown by an analysis of the residence time of the O–O axis projection on each porphyrin quadrant (Table 2). This is also reflected in the distribution of the projection of the O_b and O_t positions on the porphyrin plane, shown in Fig. 8a. The most sampled orientations correspond to regions near the staggered conformations ($\phi = \pm 45^\circ, \pm 135^\circ$). The non-symmetry of the

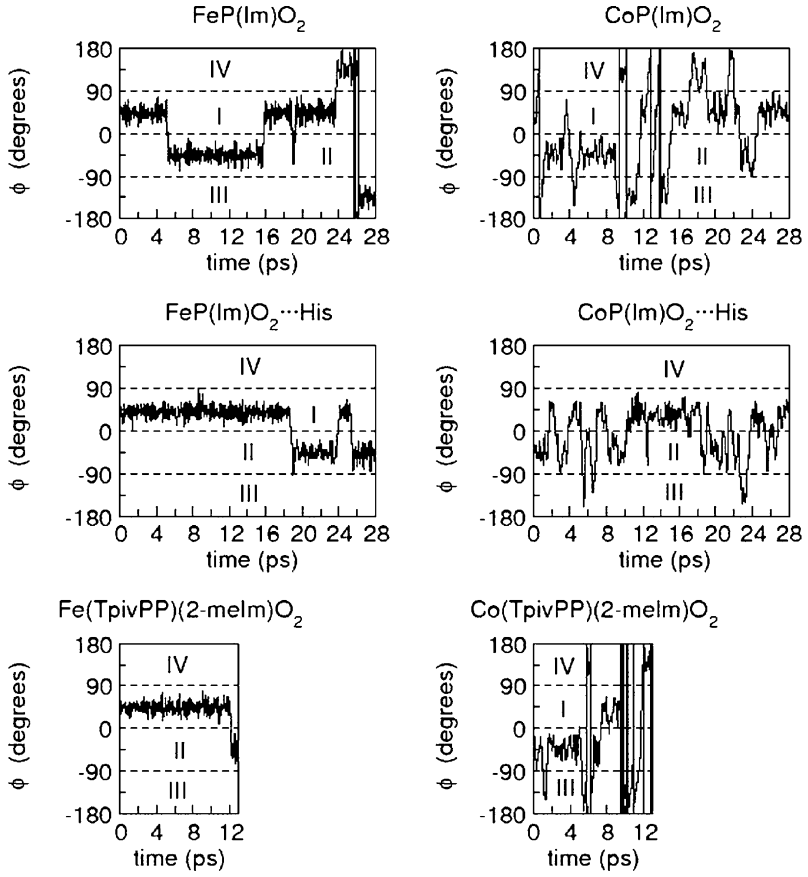

Fig. 7. Rotation of the O_2 ligand around the Me–O bond, measured as the time evolution of the ϕ dihedral angle (Fig. 5), in the six complexes investigated: $FeP(Im)O_2$, $CoP(Im)O_2$, $FeP(Im)O_2\cdots His$, $CoP(Im)O_2\cdots His$, $FeT_{piv}PP(2\text{-meIm})O_2$ and $CoT_{piv}PP(2\text{-meIm})O_2$.

Table 2
Ligand residence times on each porphyrin quadrant (**I**–**IV**), defined as the percentage of the total time in which the projection of the O_t position on the porphyrin plane lies on a given quadrant

Quadrant	$FeP(Im)O_2$	$CoP(Im)O_2$	$FeP(Im)O_2\cdots His$	$CoP(Im)O_2\cdots His$	$FeT_{piv}PP$ (2-meIm)O_2	$CoT_{piv}PP$ (2-meIm)O_2
I	25	35	78	54	93	17
II	13	13	22	40	7	44
III	19	15	0	6	0	27
IV	43	37	0	0	0	12

distribution is due to the limited time sampled in the simulation. Due to the symmetry of the system it is expected that, for longer times, the axial ligands would sample all porphyrin quadrants with equal probability.

The motion of the oxygen ligand in $CoP(Im)O_2$ is shown in Fig. 7a. Similarly to the iron complex, the O_2 ligand undergoes sizable oscillations of the ϕ angle within one porphyrin quadrant, with frequent jumps over the Fe–N_{porph} bonds. However, the frequency of these jumps is higher than in the case of the iron complex. One way to quantify the rotational dynamics of the ligand is by counting the number of times per picosecond that the O–O axis projection jumps over one Fe–N_p bond (either clockwise or anticlockwise), which defines a hopping frequency (ν_{hop}) [65] (Table 3). The hopping frequency for FeO_2 turns out to be six times smaller than that of CoO_2. In other words, the rotation of the oxygen around the metal–oxygen bond is six times faster for the cobalt analogue than for its native counterpart. This suggests that the energy barrier for ligand rotation around the metal–oxygen bond is smaller for the cobalt models. In fact, the value of the energy barrier is 1.3 kcal/mol for $FeP(Im)O_2$ but only 0.5 kcal/mol for $CoP(Im)O_2$ [23] (i.e. the rotation becomes practically barrierless for the Co complex). The fact that the Co–O bond is longer than Fe–O is probably the cause of these differences (i.e. there is less steric hindrance between the O–O bond and the Co–N_{porph} bonds). This suggests that the oxygen ligand in cobalt heme analogues will always be more flexible than their iron counterparts.

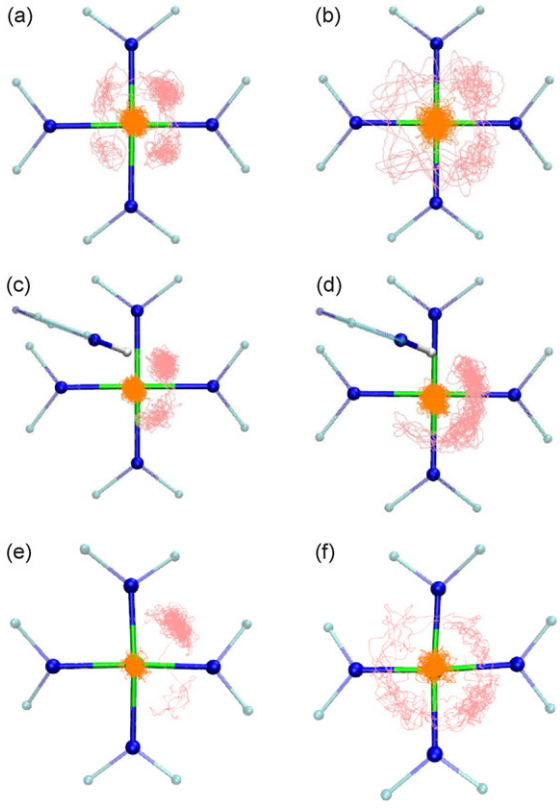

Fig. 8. Trajectory projections of the O_b and O_t atoms on the porphyrin plane. (a) $FeP(Im)O_2$, (b) $CoP(Im)O_2$, (c) $FeP(Im)O_2\cdots His$, (d) $CoP(Im)O_2\cdots His$, (e) $FeT_{piv}PP(2\text{-meIm})O_2$, and (f) $CoT_{piv}PP(2\text{-meIm})O_2$. Only the central part of the porphyrin ring (Fe, N, and C_α atoms) is shown.

3.2. *MeP(Im)$O_2\cdots$Im (Me = Fe, Co)*

Table 1 list the main parameters defining the optimized structures of the $FeP(Im)O_2\cdots His$ and $CoP(Im)O_2\cdots His$ models. As expected, the presence of the distal histidine (His64) quantitatively changes the structure of the MeO_2 fragments. The O–O distance increases (0.02 Å) and the Me–O distance also decreases (0.01 Å for Fe and 0.04 Å for Co) when His64 is present. The lengthening of O–O and shrinking of Me–O are an indication of hydrogen bond formation and can be rationalized in terms of variations in the Me–O_2 back bonding (i.e. the interaction of the d-Fe levels with the partially occupied π^* orbitals of O_2). When a positive charge approaches the ligand (such as the proton of His64), π^* orbitals are energetically stabilized. As they get closer in energy to the Fe-d orbitals, the back-bonding increases. The shift in the electron population of the orbitals (from the d-Fe orbitals to the π^* orbitals of O_2) decreases the Me–O distance and increases the O–O distance. Similar arguments have been used to rationalize the variations on the Fe–CO structure and vibrations of carbonmonoxy myoglobin [10]. The decrease of the Me–O distance is more noticeable for Co, due to the longer Co–O bond and the fact that the O_b atom is closer to

Table 3
Number of times that the O–O axis projection on the porphyrin plane crosses a Fe–N_p bond (ñ) and the hopping frequency ν_{hop}[a]

Structure	ñ	ν_{hop} (ps^{-1})
$FeP(Im)O_2$	7	0.25
$CoP(Im)O_2$	40	1.43
$FeP(Im)O_2\cdots His$	7	0.25
$CoP(Im)O_2\cdots His$	50	1.79
$FeT_{piv}PP(2\text{-meIm})O_2$	1	0.08
$CoT_{piv}PP(2\text{-meIm})O_2$	25	1.92

[a] $\nu = \tilde{n}/t_{sim}$, where t_{sim} is the simulation time.

the N_ε–H of His64 than in the case of the iron complex. These trends are independent of the two positions of the distal His given in the crystal structure (*a* and *b*) and whether the distal His is free to move or not (Table 1).

Another effect of the distal histidine is a small change in orientation of the O_2 ligand, as reflected by the decrease of ϕ (by $\approx 5^\circ$ for the iron complex and $\approx 12^\circ$ for the cobalt analogue). These variations, which increase the agreement with the X-ray structure, are due to the formation of a hydrogen bond interaction between O_2 and His64. The staggered conformation ($\phi = 45^\circ$), which is the optimum one for MeP(Im)O_2, would lead to too short a N_ε–H$\cdots$$O_t$ distance in MeP(Im)$O_2\cdots$His. Therefore, the ligand changes orientation to optimize the hydrogen bond interaction with His64. Nevertheless, the final value of ϕ is still far from the one given by experiments, suggesting that other factors such as temperature effects could affect the ligand orientation. These effects will be analyzed later on.

It is also interesting to determine the localization of the unpaired electron of the oxycobalt model and the effect of the distal histidine in its distribution. Several studies have demonstrated that the unpaired electron that gives rise to the EPR absorption of oxycobaltous proteins and compounds resides primarily on the bound oxygen [21,64,66,67]. The DFT calculations show that, indeed, the spin density is mainly concentrated on the O_2 molecule (Fig. 9), with a small contribution of the cobalt. The relative weights are 8% (Co) and 92% (O_2) in the CoP(Im)O_2 model (Fig. 9). The presence of the distal His slightly increases the relative contribution of O_2, which accounts for 95% of the total spin density. Therefore, the calculations show that the shape of the spin density distribution of oxycobalt myoglobin is an intrinsic property of the active center.

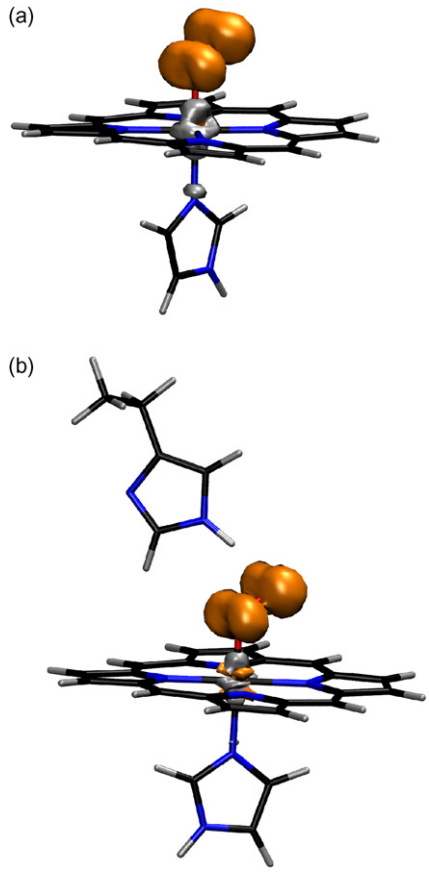

Fig. 9. Spin density distribution in (a) CoP(Im)O_2 and (b) CoP(Im)$O_2\cdots$His. Reproduced from Ref. [23], with permission of the copyright holders.

The dynamics of the oxygen ligand in the MeP(Im)$O_2\cdots$His models (Me = Fe, Co) can be also analyzed by monitoring the evolution of the N_1–Me–O_b–O_t torsional angle (ϕ). In this case, the spatial symmetry with respect to the four-porphyrin quadrants is broken with respect to the models without distal His. Therefore, independently of the length of the simulation, the ligand should not sample all porphyrin quadrants with the same probability. For instance, the interaction with His64 is maximal when the O–O projection lies on quadrant **I**, because the N_ε–H bond points in the direction of the electron density around each oxygen atom. Small rotations of His64 around the C_α–C_β and C_β–C_γ bonds could accommodate the ligand along quadrants **I** and **II**, while sampling quadrant **III** would require a larger motion of His64. On the other hand, the probability of sampling quadrant **IV** is expected to be relatively low, since the distance between the N_ε–H of His64 and the O_2 ligand would become too short, leading to a repulsive interaction, unless the His64 moves such as to increase the N_ε–H$\cdots$$O_2$ distance (e.g. by rotating around C_α–C_β and/or C_β–C_γ, defined in Fig. 2). Therefore, it is expected that the residence time of the ligand in each porphyrin quadrant would decrease in the order **I** > **II** > **III** ≫ **IV**. This is very similar to what is obtained in the simulation. As shown in Table 2 (fourth column) and Fig. 8c, only quadrants **I** and **II** are sampled for FeP(Im)$O_2\cdots$His, with residence times 78 (**I**) and 22 (**II**). The cobalt complex (Fig. 8b–d) samples more configurations than the iron complex (Fig. 8a–c) and their relative residence times, 54 (**I**), 40 (**II**), 6 (**III**) and 0 (**IV**), show the expected trend given the arguments discussed above. Interestingly, the imidazole of His64 rotates (mainly around C_β–C_α) so as to accommodate the ligand in its motion. Similar type of rotations in the picosecond time scale have been observed in classical MD simulations of carbonmonoxy myoglobin [68]. Another difference between iron and cobalt complexes is the occurrence of more configurations near the overlapping conformation ($\phi = 0$, in Fig. 6) in the case of Co. This is also reflected in the oscillations of the ϕ angle, which are larger for Co than for Fe (Fig. 7c and d), as well as in the larger values of ν_{hop} obtained for Co compared to Fe (Table 3). Therefore, the rotation of O_2 around the Me–O_2 bond is much faster for Co than for Fe. In addition, while in the iron complex the ligand shows a clear preference for the staggered conformation, in the cobalt complex it is essentially free to adopt any orientation. The limited time sampled in the simulations (28 ps) precludes computing the rate of ligand rotation, since no complete rotation of the ligand was observed. This is consistent with the experimental evidence that one full rotation every $\approx 10^4$ ps takes place [17].

As mentioned above, the Co–O–O angle reported in the X-ray analysis of $CoMbO_2$ ($109 \pm 5^\circ$) [22] is much smaller than the one reported for $FeMbO_2$ (122°) [11]. This is in contrast to the results from structure optimization, which give a Co–O–O angle only 2–3° smaller than the Fe–O–O angle (Table 1). In

addition, the computed Co–O distance is quite different (0.1 Å shorter) than the experimental one. The high flexibility of the CoO_2 unit is probably the reason of this discrepancy. Interestingly, the average value of the Co–O distance obtained from the simulation is 0.05 Å longer than the equilibrium distance, while for the iron complexes both values coincide. A similar situation occurs with the Me–O–O angles (Fig. 10). In the case of iron, the average angle is in good agreement with the X-ray structure (122°). The angle distribution is somewhat wider for Co, especially in the complexes including the distal histidine. The average angle shifts to a smaller value (119°), but is still far from the experimental data (109 ± 5°) [22]. This discrepancy could be due to the limitations of the computational approach used. It could also arise from the underestimation of the angle in the crystal structure of $CoMbO_2$ due to (a) its lower resolution with respect to the structure of $FeMbO_2$ and (b) the high flexibility of the CoO_2 unit, which precludes assigning a static orientation (a fixed value of ϕ) to the ligand [54]. The assignment becomes easier for the iron models since the ligand is less flexible. In fact, the average value of ϕ obtained from the FeP(Im)O_2···His simulation is 20.6°, which is in good agreement with the experimental value (21.5°, according to Table 1).

3.3. The interaction between the O_2 ligand and the distal histidine

The structural parameters defining the interaction between the ligand and the distal histidine in the optimized structures are listed in Table 4. In the case of iron, O_t (Fig. 2) is the oxygen atom that is closest to His, as is found in experiments. In the case of Co, the closest oxygen atom is also O_t ($O_t\cdots H < O_b\cdots H$). This is in contrast with the results of the X-ray structure which gives $O_t\cdots H > O_b\cdots H$. Nevertheless, analysis of these distances during the MD shows that there is a significant probability of finding the reverse situation ($O_t\cdots H > O_b\cdots H$) at room temperature. If we restrict our analysis to configurations in which a putative N_ε–H···O hydrogen bond is expected to be geometrically favored (H···O 2.5 Å and 140° < N_ε–H–O < 180°) [69] we find that for the iron complex the shortest interaction always involves O_t, while for the cobalt analogue this occurs 75% of the time.

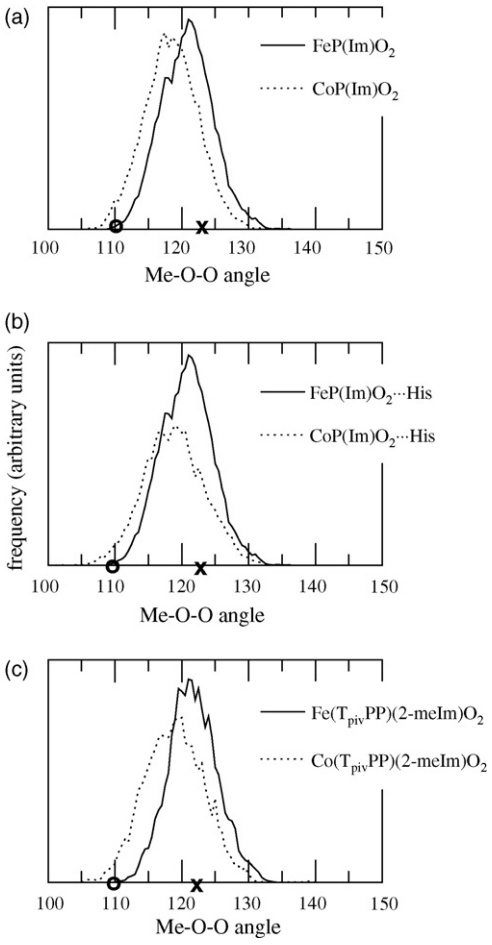

Fig. 10. Distribution of the Me–O–O angle (Me = Fe, Co) obtained from the molecular dynamics simulation. (a) MeP(Im)O_2, (b) MeP(Im)O_2···His, and (c) FeT_{piv}PP(2-meIm)O_2. The X-ray values for the Me–O–O angle are marked by a cross (Me = Fe) or an empty circle (Me = Co).

Therefore, while for the Fe complex O_t is always closer to His than O_b, both scenarios ($H\cdots O_t < H\cdots O_b$ and $H\cdots O_t > H\cdots O_b$) are possible for the cobalt complex. This is in agreement with the X-ray structure of oxycobalt myoglobin, in which O_b is closer to His than O_t [22]. Even though this is not the most sampled configuration observed in the simulation, it has a sig-

Table 4
Hydrogen bond parameters corresponding to the optimized structures of the MeP(Im)O_2···His complexes (Me = Fe, Co)

Model	<N_ε–H···O_t	<N_ε–H···O_b	N_ε–H	$O_b\cdots N_\varepsilon$	$O_t\cdots N_\varepsilon$	$O_b\cdots HN_\varepsilon$	$O_t\cdots HN_\varepsilon$
FeP(Im)O_2···His	160.2	135.1	1.04 (a)	3.03 (a)	2.72 (a)	2.27 (a)	1.72 (a)
	171.1	138.1	1.04 (b)	3.12 (b)	2.79 (b)	2.17 (b)	1.76 (b)
FeP(Im)O_2···His *free*	160.2	135.1	1.04	3.32	2.87	2.50	1.87
exp ($FeMbO_2$)[a]	142.5[b]	113.6[b]	–	3.02 (a)	2.67 (a)	–	–
	160.1[b]	136.8[b]		3.08 (b)	2.97 (b)	–	–
CoP(Im)O_2···His	169.6	135.1	1.04	3.10	2.79	2.27	1.76
CoP(Im)O_2···His *free*	170.2	139.5	1.04	3.30	2.87	2.44	1.85
exp ($CoMbO_2$)[c]	171.7[a]	139.9 [a]	–	2.72	3.01	–	–

Distances are given in angstroms and angles in degrees.
[a] Ref. [11].
[b] Value obtained on adding a hydrogen atom to the N_ε of His64.
[c] Ref. [22].

nificant probability to take place, something that does not occur for the iron complex. On the other hand, the fact that the analysis of the equilibrium structures leads to different conclusions illustrates the need to take into account dynamical effects in order to interpret the experimental data for highly flexible units such as the CoO_2 fragment.

It is interesting to relate the above distance analysis with the occurrence of a hydrogen bond interaction between His and O_2. Several studies in both iron and cobalt myoglobin and hemoglobin have demonstrated that there is a hydrogen bond between the terminal oxygen and the N_ε-bound proton on the imidazole of the distal histidine [13,17,70,71]. Although this interaction is believed to be an important factor in controlling oxygen affinity [72], the strength of the hydrogen bond for both metal complexes remains controversial. While photolysis experiments suggested that there is a stronger hydrogen bond to the distal histidine in $FeMbO_2$ versus $CoMbO_2$ [73], the reverse was predicted by calculations on the cobalt picket fence porphyrin using a parameterized interaction potential [74]. In addition, it is not known whether the hydrogen bond interaction involves either both oxygen atoms or only one of them.

Our calculations give a value of 3.7 kcal/mol for the hydrogen bond interaction between the oxygen ligand and the distal His in $FeP(Im)O_2\cdots$His. This value is similar to the ones reported in previous DFT investigations [9,10,75]. There is no theoretical data available for the hydrogen bond energy of the cobalt analogue. Nevertheless, given the superoxide anion like character of the oxygen ligand (i.e. Co^{3+}–$O_2{}^-$, as reflected in the fact that the spin density distribution is mainly localized on the oxygen molecule), it is expected that CoO_2 forms a stronger bond with His64. In fact, we obtained a value of 4.7 kcal/mol for the hydrogen bond interaction in $CoP(Im)O_2\cdots$His. An obvious question at this point is why does the ligand rotate around the Me–O bond given the relatively strong His$\cdots O_2$ interaction in the equilibrium structure. The answer to this question can be related to the different mobility of the two oxygen atoms in the dynamics and its role in the hydrogen bond interaction. As shown in Fig. 8, the terminal oxygen atom (O_t) moves around the porphyrin quadrants, eventually losing the interaction with His. Instead, the bridging oxygen atom (O_b) is confined in a small region around the equilibrium position, thus keeping the interaction with His during the whole trajectory. This indicates that the bridging oxygen is responsible for keeping the hydrogen bond interaction during the rotational motion of the ligand, while the position of O_t is less relevant.

In summary, our calculations give support to previous studies on the existence of a hydrogen bond interaction between the bound ligand and the distal histidine [13,17,70,71]. We show that this interaction is due to the bridging oxygen atom and predict that it is somehow weaker for the native iron system than for the cobalt analogue. In addition, the rotational motion of the oxygen around the Me–O bond is faster for Co than for Fe. Therefore, we show that both the affinity and dynamics of ligands in cobalt-based heme proteins is different than iron-based. This difference may have implications in practical work on artificial enzymes or heme-based sensors [76].

3.4. $MeT_{piv}PP(2\text{-}meIm)O_2$ (Me = Fe, Co)

The "picket-fence" strategy is one of the most successful approaches to build heme models [15]. In this approach, the porphyrin is functionalized with bulky groups in order to ensure the selective binding of an axial base (usually an alkyl imidazole or pyridine) and a diatomic molecule (e.g. O_2, CO) to the iron atom. In so doing these models mimic the stereochemical properties of myoglobin and hemoglobin and have oxygen affinities similar to the values measured for heme proteins [77]. The first heme model that reversibly binds oxygen [i.e. the *picket-fence-oxygen* complex $Fe(T_{piv}PP)(1,2\text{-}MeIm)(O_2)$] was obtained in the early 70′s by Collman and coworkers ($T_{piv}PP$ = tetrapivalaminophenyl porphyrin; 1,2-meIm = 1,2-methylimidazole) [15]. The research on synthetic models of the protein has led to a deeper understanding of the ligand-binding properties of myoglobin. For instance, several studies have shown that structural differences among heme models are able to vary the equilibrium constant (K_{eq}) of the O_2 and CO binding reaction. These changes have been attributed mainly to hydrogen bonding and polar interactions [78–83], but steric interactions, porphyrin distortions and the interplay of various factors have also been proposed [84,85].

X-ray structures of picket-fence-oxygen complexes commonly show a fourfold disorder of the bound O_2 [15,16,77,86], something that has been interpreted as a dynamic O_2 motion [79–81]. The structure of the iron-picket-fence-oxygen complex was previously studied [63]. The dynamics of this complex is reported here, in comparison with its cobalt analogue. The most relevant parameters of the optimized structures of $MeT_{piv}PP(2\text{-}meIm)O_2$ (Me = Fe, Co) are shown in Table 1. Similarly to $MeP(Im)O_2$, the ligand shows a staggered orientation with respect to the Me–N bonds, where N are porphyrin ring atoms. The discrepancy in the length of the Me–N_{ax} bond can be attributed to the steric interaction with the 2-methyl substituent, not present in $MeP(Im)O_2$.

The dynamics of the O_2 ligand in $MeT_{piv}PP(2\text{-}meIm)O_2$ were analyzed in a similar way as the $MeP(Im)O_2$ and $MeP(Im)O_2\cdots$His complexes (Sections 3.1 and 3.2). The frequency distribution of the Me–O–O angle (Fig. 10) shows again that the average angle is larger for the iron complex (123°) than for the cobalt analogue (120°). In the case of the iron complex, only two porphyrin quadrants (**I** and **II**) were sampled (Fig. 8), reflecting that there is a barrier for the transition over porphyrin quadrants. Instead, the O_2 ligand in the cobalt complex samples all porphyrin quadrants in about 8 ps. Therefore, the dynamics of the ligand display features that resemble $MeP(Im)O_2$ and $MeP(Im)O_2\cdots$Im. The values of the hopping frequencies are not directly comparable since the simulation time is different in each case (14 ps for the larger picket systems and 25 ps for the small heme models). However, it is clear from Fig. 7 that the oxygen ligand in the cobalt analogue is more mobile than the iron complex.

Comparison of our results (hopping frequencies) with the experimental data (rate of rotation) is not straightforward, because only those hops leading to a complete cycle rotation

Table 5
Selected structural parameters of the MeCbl and AdoCbl molecules in comparison with X-ray data

Parameter	MeCbl (calc.)	AdoCbl (calc.)	MeCbl (exp.)[a]	AdoCbl (exp.)[b]
Co–C	1.99	2.02	1.98	2.03
Co–N_{ax}	2.15	2.16	2.16	2.24
Co–N_c (aver.)[c]	1.87, 1.93	1.86, 1.93	1.88, 1.95	1.87, 1.91
N_c–C	1.34–1.45	1.31–1.51	1.32–1.49	1.31–1.50
<Co–C–C	–	126.4	–	123.4
<C–Co–N_{ax}	175.1	170.9	171.1	171.3
<N_c–Co–N_{ax}	87.3–95.2	86.3–95.2	85.7–94.8	86.1–94.8
<C–Co–N_c	88.1–92.2	82.5–90.5	86.3–94.8	84.0–93.2
δN_c–C_1–C_2–N_c	40.8	41.0	41.7	38.4
Fold angle (α)	13.3	13.5	13.6	14.3

[a] Ref. [105].
[b] Ref. [106].
[c] Average values corresponding to short and long equatorial Co–N bond lengths.

around Me–O contribute to the measured rotational rate. In the case of $CoP(Im)O_2$, we observed three complete rotations of the ligand during the total simulation time (28 ps), while for $FeP(Im)O_2$ we only found one. This gives a rate of rotation of 10^{-1} cycles/ps (Co) and 4×10^{-2} (Fe), again reflecting the faster motion of Co with respect to Fe. These values should be considered as approximate, as our simulation is not long enough to give a reliable value for the rate of rotation. Nevertheless, the higher value we obtain compared to experiment (10^{-4} cycles/ps in $CoHbO_2$) [17] is probably due to the absence of hydrogen bond interaction between the ligand and the distal His, which is expected to slow down the rotational motion of the ligand. Therefore, our results predict that for a non-interacting MeO_2 unit, the ligand will be rotating at a rate of $\approx 10^{-1}$ cycles/ps (Co model) and $\approx 10^{-2}$ cycles/ps (Fe model).

4. Structure and dynamics of B_{12} models

4.1. Methylcobalamin and adenosylcobalamin

The molecules of MeCbl and AdoCbl (Figs. 4 and 5) act as cofactors of enzymes involved in several relevant biological reactions [25–31], such as the interchange of a functional group (e.g. alkyl fragment, –OH or $–NH_2$) and a hydrogen. Their structural properties have been recently reviewed [33]. From a theoretical point of view, the structures of MeCbl and AdoCbl have been studied during the last decade using small models including the corrin ring and the axial ligands (Ado and dimethylbenzimidazole, DMB, in the case of AdoCbl and CH_3 and DMB in the case of MeCbl). Most of these studies are focused on reproducing the Co–C and Co–N_{ax} bond lengths and the experimental Co–C bond dissociation energy (BDE $\approx$ 31 kcal/mol for AdoCbl, and $\approx$36 kcal/mol for MeCbl). It was early recognized that these systems represent a challenge for theoretical modeling since it was not possible to reproduce the experimental Co–C BDE nor the Co–N_{ax} distance. The first problem (the disagreement between experimental and calculated BDE values) was found to be partially due to the use of the B3LYP exchange-correlation functional [87]. DFT calculations using BP86 functional increased the agreement with experiment (the BDE is about 8 kcal/mol larger with respect to B3LYP values), but there was still a 4–5 kcal/mol difference between theory and experiment. Solvent effects and the conformational freedom of the Ado fragment have been put forward to explain this issue [88,89]. Concerning the second problem, the Co–N_{ax} distance, it was recently found that taking into account the complete MeCbl cofactor [90] reproduces this bond length (Table 5). In the case of AdoCbl, however, calculations using the complete cofactor did not yet reproduce the experimental value (Table 5). This was found to be due to intermolecular interactions involving the Ado axial group. The unit cell of either the MeCbl or the AdoCbl crystal contains four closely packed cofactor molecules and a number of water molecules. In the case of MeCbl, there are practically no interactions between the Me axial ligand and the nearest neighbor molecules. However, the more voluminous Ado group of AdoCbl is involved in a number of intermolecular interactions with water molecules and, more importantly, with the side chains of neighboring molecules. Recent DFT calculations on the AdoCbl crystal [91] show a good agreement of the Co–N_{ax} distance with experiments, underlining the influence of intermolecular interactions in the value of this distance. In contrast, the more robust Co–C axial bond length was found not to be influenced by such intermolecular interactions.

The mutual influence of the two axial bonds in MeCbl and AdoCbl has also been studied using DFT [90]. Experimentally, it is known that the binding of one axial ligand weakens the bond of the other, i.e., the Co–C binding energy decreases when the DMB ligand is bound on the other side of the corrin ring. Conversely, the Co–N_{ax} binding energy is smaller when the Ado or CH_3 axial ligands are present. This situation is somewhat different from what is found in other biologically relevant metal-macrocycles containing an $M\{d^6\}$ cation in an octahedral environment. In the hemeproteins myoglobin and hemoglobin, for instance, the synergy between the two heme axial ligands (O_2 and His) is well documented [55,92]. DFT calculations on MeCbl gave further support to this conclusion [90]. An opposite effect of the two axial ligands was observed: the alkyl ligand strengthens the bond of the axial base, while the axial base weakens the bond with the alkyl ligand. The opposite effect of the two axial ligands can be rationalized with a simple orbital picture. There are two occupied orbitals that mainly contribute to the Co–C and Co–N_{ax} bonds in MeCbl (Fig. 11). The lowest energy orbital is

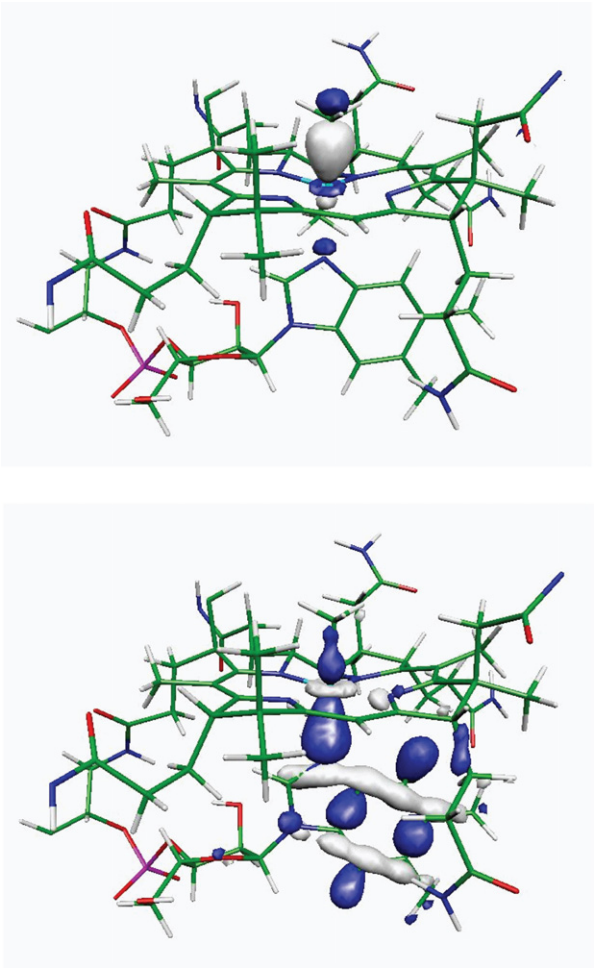

Fig. 11. Isosurface plots of the two occupied orbitals that mainly contribute to the Co–C (top) and Co–N_{ax} (bottom) bonds in MeCbl. Reprinted with permission from Ref. [90]. Copyright (2004) American Chemical Society.

a σ^{CH_3}–dz^2–σ^{BZM} bonding orbital, being mostly weighted on σ^{BZM}. The second orbital lies higher in energy and it is only bonding with respect to the Co–C bond. DFT calculations show that a slight elongation of the Co–C bond (by 0.15 Å) raises the energy of both orbitals, thus weakening the Co–N bond. In the extreme case of the homolytic cleavage of the Co–C bond, the weakening of the Co–BZM bond simply reflects the change in oxidation state of the Co center from +3 in MeCbl to +2 in the methyl-off form. As the extra electron on the Co center in the met-off form localizes in the Co$\{dz^2\}$-derived molecular orbital (that is antibonding with respect to the Co–N_{ax} bond) the Co–N_{ax} bond weakens with respect to MeCbl. In contrast, elongation of the Co–N_{ax} bond changes the energy of the two orbitals in opposite directions, therefore the effect of stretching the Co–N_{ax} bond is less pronounced. This simple argument, already introduced by Mealli et al. [93], explains why the alkyl ligand influences significantly the bond of the axial base, while the axial base has a minor effect on the Co–C bond. Note that this is different from the well-known trans effect observed upon change of the alkyl and axialbase ligands [35]. A similar model is proposed by Stich et al. in a recent analysis of cobalamins using time-dependent density-functional theory (TD-DFT) [94]. Therefore, DFT provides quantitative support to these previously proposed models.

In summary, the DFT analysis of AdoCbl and MeCbl shows that a good agreement with experiment can be obtained using small models, but to reproduce the Co–N_{ax} distance it is necessary to take into account the full coenzyme (MeCbl) or the complete molecule in its crystalline environment (AdoCbl). The analysis of the electronic structure evidences an opposite effect of the axial ligands in MeCbl (the same arguments are expected to hold for AdoCbl): the CH_3 ligand significantly reinforces the bond with the axial base, while the axial base slightly weakens the Co–C bond. This is in agreement with experimental studies showing that the Co–C bond is stronger for the *base-off* form [95–98] and suggest that interconversion between *base-on* and *base-off* forms of the cofactor in MeCbl-dependent enzymes will have little effect on the strength of the Co–C bond. DFT and molecular dynamics are thus promising techniques to elucidate the problems related to the cleavage of the Co–C bond in MeCbl and AdoCbl in the protein. Several studies on this line have recently appeared [99,100].

4.2. Organocobalt complexes

Organocobaloxime derivatives are often used as models for the B_{12} coenzyme. Most of them have the formula $Co(dmgH)_2(L)R$ where dmgH is the monoanion of dimethylglyoxime, L is an axial base and R is an organoligand. The protonation state of the dimethylglyoxime ligands (dmg^{2-}, $dmgH^-$ or $dmgH_2$) can be identified by a slight lengthening of the Co–N and N–O distances of the protonated NO unit with respect to the unprotonated one. This is the case, for instance, of the cobaloxime complexes $[Co(dmgH)_2(H_2O)(NO_2)$ and $Co(dmgH)_2(Cl)(4\text{-chloroaniline})\cdot 2H_2O]$. As a first step in our study, we performed calculations on these two complexes. Our calculations on the crystalline form of $Co(dmgH)_2(Cl)(4\text{-chloroaniline})\cdot 2H_2O$ (Table 6) are in good agreement with experiment [38]. They also show that the asymmetric $dmgH_2/dmg^{2-}$ arrangement is stabilized by the formation of hydrogen bond interactions between the oxime ligands and the solvent water molecules. In fact, calculations in the absence of solvent molecules lead to the symmetric $(dmgH)_2$ configuration. In the case of $Co(dmgH)_2(H_2O)(NO_2)$, neutron diffraction measurements [37] unambiguously show that the two dimethylglioxyme ligands have a different protonation state ($dmgH_2$ and dmg^{2-}). The optimized structure of the crystal (Table 6) is also in very good agreement with experiment. In this case, the asymmetric $dmgH_2/dmg^{2-}$ arrangement is found to be stabilized by the formation of strong hydrogen bond interactions among the cobaloxime molecules. In particular, the NO oxygen of one oxime ligand interacts with the hydrogen atom of the H_2O ligand of its neighboring molecule in the crystal. Alltogether, our results highlight the importance of intermolecular interactions in dictating the protonation state of the equatorial ligands in cobaloxime derivatives.

Very often, however, the assignment of the protonation state of the oxime ligands from the structural data alone is not possible, either because the position of the

Table 6
Optimized structural parameters for the organocobaloxime crystals $[Co(dmgH)_2(Cl)(4\text{-chloroaniline})\cdot 2H_2O]$ and $Co(dmgH)_2(H_2O)(NO_2)$[a]

Distance	$Co(dmgH)_2(Cl)(4\text{-chloroaniline})\cdot 2H_2O$ calc. (exp.)[b]	$Co(dmgH)_2(H_2O)(NO_2)$ calc. (exp.)[c]
Co–R[d]	2.24 (2.26)	2.04 (2.00)
Co–L	2.03 (2.00)	1.89 (1.90)
O···O	2.48/2.49 (2.48/2.50)	2.51 (2.50)
H···O	1.39/1.41 (–)	1.44 (1.47)
O–H	1.09/1.10 (–)	1.08 (1.04)
Co–N	1.88/1.90 (1.88/1.91)	1.89/1.90 (1.90)
N–O	1.33/1.35 (1.33/1.35)	1.34/1.36 (1.32/1.34)
N–C	1.31 (1.29/1.31)	1.30/1.31 (1.29)
C–C	1.46 (1.46)	1.46 (1.47)
$C–CH_3$	1.49 (1.49)	1.49 (1.48)

Distances are given in angstroms and angles in degrees.
[a] When two different values for the same distance were found, both results are given, except when they differ by less than 0.01 Å. In this case the average value is given.
[b] Ref. [38].
[c] Ref. [37].
[d] R = Cl, L = 4-chloroaniline for $Co(dmgH)_2(Cl)(4\text{-chloroaniline})\cdot 2H_2O$; $R = H_2O$, $L = NO_2$ for $Co(dmgH)_2(H_2O)(NO_2)$.

hydrogen atoms is not available or because the change in the Co–N and N–O distances is very small. This is the case, for instance, of the organocobaloxime crystal $[Co(CCl{=}CHCl)(dmgH)_2(py)].CHCl_3$ (i.e., L = pyridine, R = CCl=CHCl), shown in Fig. 12 [39], which we investigated in detail [101].

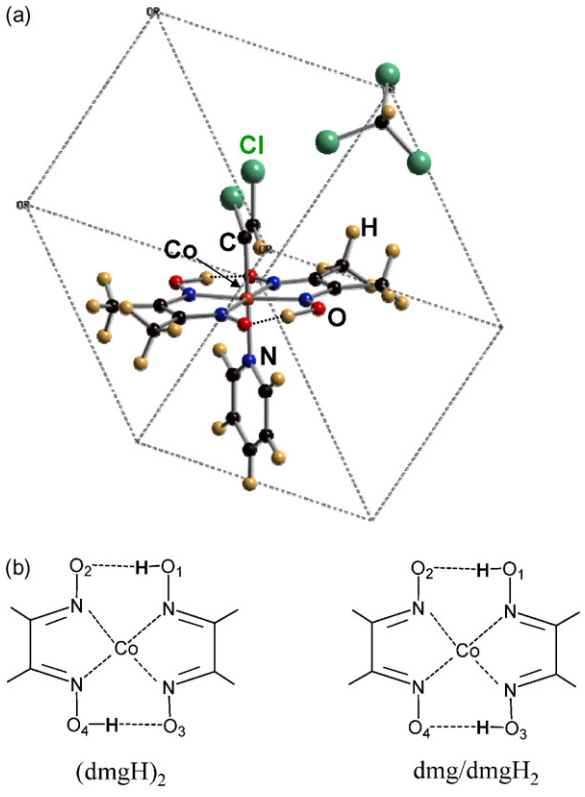

Fig. 12. (a) Unit cell of the $Co(CCl{=}CHCl)(dmgH)_2(py)$ crystal. (b) Atom numbering of the equatorial ligands.

Table 7
Optimized structural parameters for the organocobaloxime crystal $Co(CCl{=}CHCl)(dmgH)_2(py)$. Only the $(dmgH)_2$ arrangement is stable for crystal form I[a]

Distance[b]	Crystal form **I**	Crystal form **II**		X-ray[c]
	$(dmgH)_2$	$(dmgH)_2$	$dmg/dmgH_2$	
Co–R	1.95	1.95	1.94	1.96
Co–L	2.00	2.00	2.01	2.03
O···O	2.48/2.50	2.48/2.50	2.49	2.49
H···O	1.40/1.42	1.37/1.43	1.39/1.41	–
O–H	1.10	1.11/1.08	1.11/1.09	–
Co–N (A)	1.87/1.89	1.87/1.89	1.89	1.89
Co–N (B)	1.88/1.89	1.88/1.89	1.87	1.89
N–O (A)	1.32/1.36	1.32/1.37	1.35	1.34
N–O (B)	1.32/1.36	1.32/1.35	1.32	1.34
N–C (A)	1.31	1.31	1.31	1.29
N–C (B)	1.31	1.31	1.32	1.30
C–C (A)	1.45	1.45	1.46	1.46
C–C (B)	1.45	1.45	1.45	1.47
C–Ca	1.49	1.49	1.49	1.49
C–Cb	1.49	1.49	1.49	1.48

Distances are given in angstroms and angles in degrees.
[a] When two different values for the same distance were found, both results are given, except when they differ by less than 0.01 Å. In this case the average value is given.
[b] R = CCl=
CHCl; L = pyridine; A, B = the two equatorial ligands.
[c] Ref. [39].

Our calculations for an isolated $Co(CCl{=}CHCl)(dmgH)_2(py)$ molecule show that both $(dmgH)_2$ and $dmg/dmgH_2$ arrangements (Fig. 12b) are stable, but the $(dmgH)_2$ form is energetically the most favored (by 2 kcal/mol). The situation is different for the molecule in the crystalline phase (Table 7). Since there are two orientations of the solvent molecule of the crystal, one optimization was performed for each crystal form (**I** and **II**). Surprisingly, the asymmetric $dmg/dmgH_2$ arrangement is not a stable minimum for crystal form **I**. However, both arrangements are stable in crystal form **II** and, moreover, they are practically isoenergetic (their energy difference is less than 0.3 kcal/mol). It appears that the less favored $dmg/dmgH_2$ form is stabilized in the crystal by weak C–H···O=N interactions. In other words, subtle changes in the C–H···O=N interactions can determine the protonation state of the dimethylglyoxime ligands. In view of the relatively low barrier for the proton transfer in the O···H···O units [102], it is expected that both $(dmgH_2)$ and $dmg/dmgH_2$ forms contribute to the dynamics of the crystal at a given temperature.

In order to analyze the effect of the temperature on the protonation state of the dimethylglyoxime ligands, a series of AIMD simulations on the $[Co(CCl{=}CHCl)(dmgH)_2(py)]\cdot CHCl_3$ crystal were performed. Two different temperatures were considered, 173 K (the temperature of the crystal structure determination [39]) and 300 K (most of the B_{12} mimetics based on dimethylglyoxime are crystallized at room temperature). The molecular dynamics simulations at 173 K on the crystal form A show that the bridging protons often jump from one dimethylglyoxime ligand to another. This leads to a delocalization of the protons, as it is evidenced in the probability distribution of the

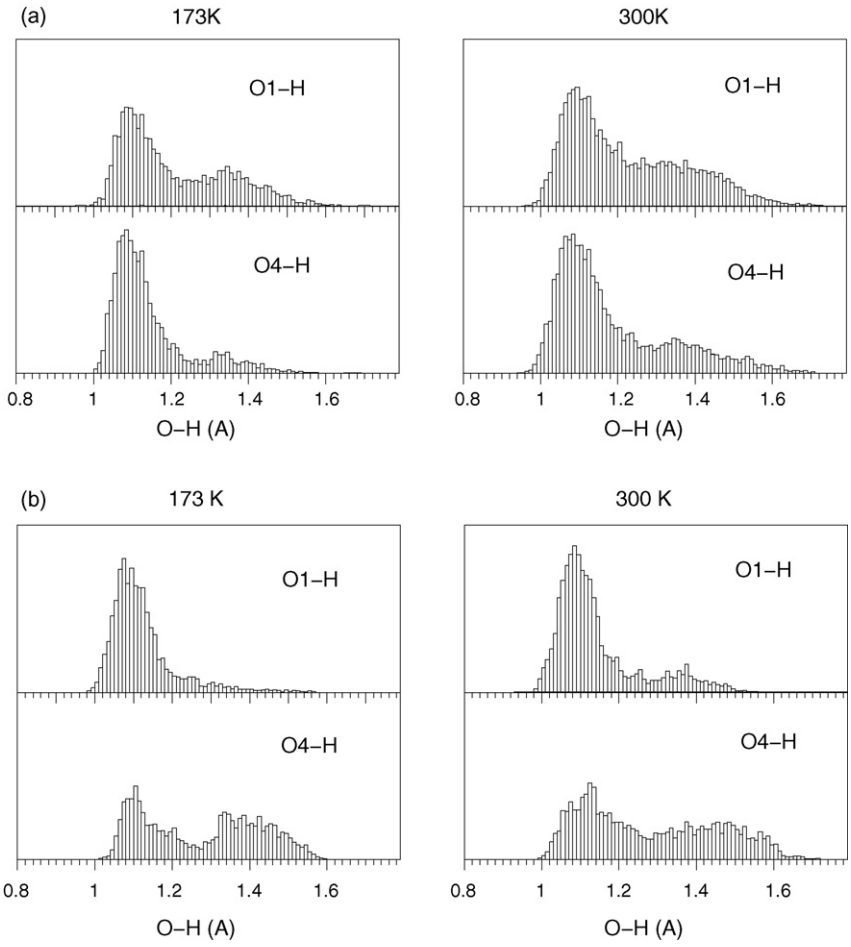

Fig. 13. (a) Probability distribution of the O1–H and O4–H bond lengths (see atom numbering in Fig. 12) in crystal form **I** of [Co(CCl=CHCl)(dmgH)$_2$(py)]·CHCl$_3$ at (a) 173 K and (b) 300 K. (b) Same distributions for crystal form **II**. Reprinted with permission from Ref. [101]. Copyright (2002) American Chemical Society.

O–H distances. Fig. 13 shows that there is a well-defined maximum at 1.09 Å for both O_2–H and O_2–H distributions, while longer O–H distances have a relatively low population even at 300 K. Analysis of the correlation between both O–H distances shows that the $(dmgH)_2$ arrangement is the dominant one. This picture is consistent with the results of the structural optimizations which showed that the $(dmgH)_2$ form is the only minimum. Another feature that comes out of Fig. 13 is that O_1–H is more delocalized into larger distances than O_4–H, at both temperatures. An explanation for this can be found by relating these distances with the intermolecular interactions affecting the oxime oxygen atoms in each case. The short Cl_3C–H···O=N interaction acting on O_2 (Fig. 14a) favors the protonation of O_4, which makes the O_2–H···O_4 configurations (i.e. longer H···O_4 bonds) less probable than the O_3···H–O_4 ones.

The corresponding distance distributions for crystal form **II** is shown in Fig. 13b. The O_1–H distribution shows a maximum at 1.1 Å, exactly as in the crystal form A (Fig. 13a), but there is little population for larger distances. Fig. 14b shows that in this case the short Cl_3C–H···O=N interaction acts on O_2, favoring the short O_1–H distances. As a consequence, the O_1–H distribution resembles that of O_4–H in crystal form **I** (Fig. 13a). On the other hand, the distribution of O_4–H appears quite different from the ones analyzed up to now. It has two maxima, localized at 1.1 and 1.4 Å, both with a similar population. This is consistent with the results of the structural optimizations which showed both $(dmgH)_2$ and dmg/$dmgH_2$ arrangements to be isoenergetic. Note that the difference between both situations is in the position of the O_4···H···O_3 proton. Therefore, the bridging proton of the O_4···H···O_3 unit (Fig. 14b) can be considered as equally shared among both oxygen atoms, and described as a low energy barrier hydrogen bond.

These results have important implications for the assignment of a protonation state to the dimethylglyoxime ligands of the B_{12} mimetic Co(CCl=CHCl)$(dmgH)_2$(py). First of all, one of the bridging protons can be associated essentially with one of the oxime oxygen atoms, while a second proton cannot be assigned to merely one oxygen atom. Together with the structural results, which showed the existence of several minima very close in energy, this explains why it is not possible to identify the protonation state of the dimethylglyoxime ligands unambiguously. Even at 173 K, one of the bridging protons is delocalized among both oxime oxygen atoms. The crystal structure actually reflects the behavior of the system, for it is an average among all possible structural conformations.

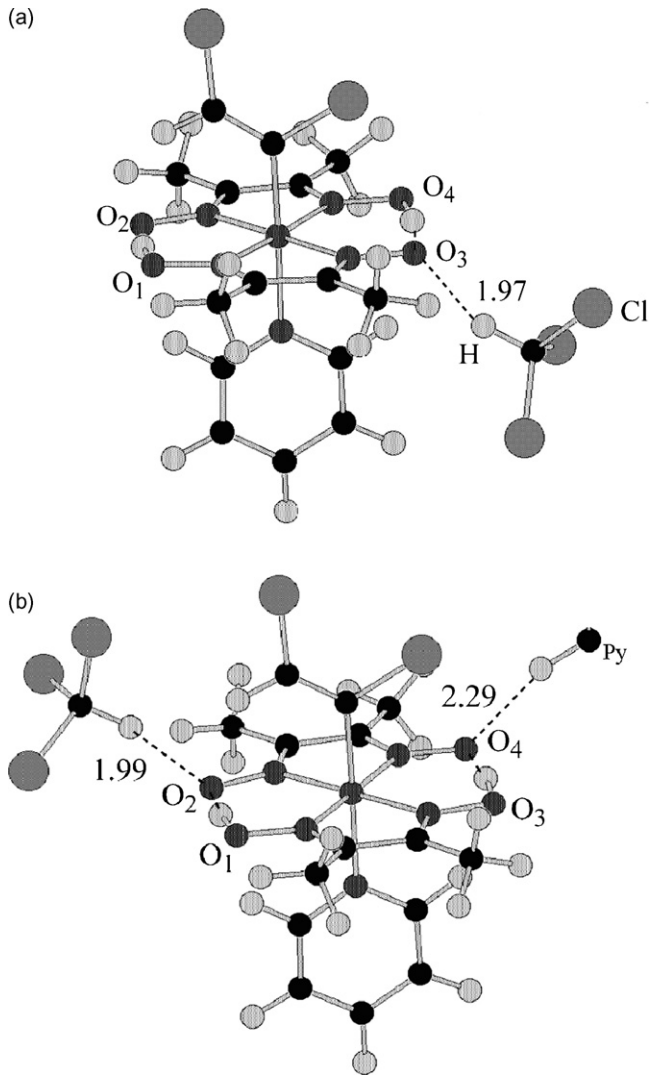

Fig. 14. Shortest intermolecular interactions involving the oxime oxygen atoms in the optimized structure of (a) crystal form **I** and (b) the dmg/dmgH$_2$ isomer of crystal form **II**. Reprinted with permission from Ref. [101]. Copyright (2002) American Chemical Society.

5. Summary and conclusions

This work focuses on the structure and dynamics of equatorial and axial ligands in biologically relevant iron and cobalt complexes with macrocyclic ligands. Three examples are shown, related either to models of the oxygen binding proteins hemoglobin and myoglobin (iron-based), or models of the B_{12} coenzyme (cobalt-based). Density-functional theory (DFT) calculations, combined with DFT-based molecular dynamics simulations (AIMD), are performed in order to complement experimental studies of these complexes. The simulations allow the evolution of the system to be followed for a short time interval of time at finite temperature.

The first example summarizes our recent study of the dynamics of the metal–ligand bond in heme models and its cobalt analogues [23]. Several models are considered: MeP(Im)O_2 and MeP(Im)$O_2\cdots$Im (Me = Fe, Co; Im = imidazole; P = porphyrin), as well as the picket-fence oxygen molecules MeT_{piv}PP(2-meIm)O_2 (Me = Fe, Co). The results of the molecular dynamics simulation show that in all cases the oxygen ligand undergoes a fast rotational motion around the metal–oxygen bond. The mechanism is fully consistent with the interpretation of previous experimental studies of heme analogues [17,18], providing a detailed picture of the dynamics of these highly flexible metal–oxygen bonds. Even though both cobalt and iron models follow this general picture, there are quantitative differences. Firstly, the rotational motion of the oxygen around the Me–O bond is faster for Co than for Fe. Secondly, the interaction of the ligand with the distal His is stronger for the cobalt complex (4.7 kcal/mol) than for the iron one (3.7 kcal/mol). There are also differences concerning which oxygen atom is the best hydrogen bond acceptor. Finally, a word of caution is raised with respect to drawing conclusions from static calculations for these highly flexible metal–ligand bonds.

The second example deals with the cobalt–axial ligand bonds (Co–C and Co–N_{ax}) in B_{12} cofactors (AdoCbl and MeCbl). Both the binding energy of the Co–C bond and the length of the Co-axial base (dimethylbenzimidazole) in B_{12} cofactors have proven to be elusive for density-functional methods [103], but recent studies show that using the adequate exchange-correlation functional and considering the full cofactor in the calculations solve these discrepancies [87,90,91]. Furthermore, it has been demonstrated that the value of the Co–N_{ax} distance in the AdoCbl crystal is affected by intermolecular interactions [91]. The mutual influence of both axial ligands, analyzed in the case of MeCbl, evidences an opposite effect of the axial ligands: the alkyl ligand significantly reinforces the bond with the axial base, while the axial base slightly weakens the Co–C bond. This is in agreement with experimental studies showing that the Co–C bond is stronger for the *base-off* form [95–98], and suggest that interconversion between *base-on* and *base-off* forms of the cofactor in MeCbl-dependent enzymes will have little effect on the strength of the Co–C bond.

The third example shown focuses on the oxime ligands in organocobaloxime mimetics of the B_{12} coenzyme. The protonation state of the equatorial oxime ligands ($dmgH^-$ or $dmgH_2$) can be identified from the length of the Co–N and N–O distances. However, very often variations on these distances are too small to allow the identification of the protonation state from crystallographic data alone. This is the case, for instance, of the [Co(CCl=CHCl)$(dmgH)_2$(py)].$CHCl_3$ cobaloxime complex, which was here analyzed in detail. The methodology used was tested by performing calculations on two organocobaloxime complexes for which the protonation state is known experimentally [Co$(dmgH)_2$(Cl)(4-chloroaniline)$\cdot 2H_2O$ and Co$(dmgH)_2(H_2O)(NO_2)$]. In the latter, the protonation state is known from neutron diffraction measurements [37], whereas in the former it is inferred from the length of the Co–N and N–O distances [38]. In both cases, our results turned to be in good agreement with experiment, confirming that the Co–N and, more importantly, the N–O distances are related to the protonation state of the cobaloxime ligands. A more thoughtful analysis was performed for [Co(CCl=CHCl)$(dmgH)_2$(py)].$CHCl_3$, as in this case the protonation state of the equatorial ligands is not known experimentally [39]. We found that the most stable

arrangement for an isolated molecule is the $(dmgH)_2$ one. In the crystal, however, the weak C–H···O intermolecular interactions between the solvent and the oxime oxygen atoms are enough to change this situation. Our simulations [101] show that one of the bridging OH···O protons can be essentially associated to one oxime oxygen, while the proton of the second dimethylglyoxime ligand is essentially shared between the two oxygen atoms, explaining the absence of a clear signature of the protonation state of the dimethylglyoxime ligands in the structural determination. The fact that small changes in the directionality of weak intermolecular interactions can contribute to the delocalization of the oxime protons is at variance with the common assumption that only strong hydrogen bonds can stabilize the dmg/$dmgH_2$ configuration [104], as happens in $Co(dmgH)_2(Cl)$(4-chloroaniline)·$2H_2O$ [38] and $Co(dmgH)_2(H_2O)(NO_2)$ [37]. This could have implications in the synthesis of cobaloxime biomimetics with the desired dimethylglyoxime arrangement.

Acknowledgements

This work was supported by the *Generalitat de Catalunya* (grant 2005SGR-00036), the *Spanish Ministry of Science and Education* (grant FIS2005-00655) and the *Academy of Finland* (Center of Excellence Grant 2006-2011). We thankfully acknowledge the computer resources, technical expertise and assistance provided by the Barcelona Supercomputing Center, Centro Nacional de Supercomputación and by the M-grid project of the Helsinki University of Technology. We are grateful to M. Parrinello, K. Kunc, P. Ordejón and P. M. Kozlowski for discussions and collaboration concerning this work.

References

[1] I. Bertini, H.B. Gray, S.J. Lippard, J.S. Valentine, Bioinorganic Chemistr, University Science Books, Mill Valley, CA, 1994.
[2] L. Stryer, J.M. Berg, J.L. Tymoczko, Biochemistry, 6th ed., W. H. Freeman, 2007 (Chapter 7).
[3] F. Schotte, M. Lim, T.A. Jackson, A.V. Smirnov, J. Soman, J.S. Olson, G.N. Phillips Jr., M. Wulff, P.A. Anfinrud, Science 300 (2003) 1944.
[4] J.H. Wang, A. Nakahara, E.B. Fleischer, J. Am. Chem. Soc. 80 (1958) 1109.
[5] B. Stec, G.N. Phillips Jr., Acta Crystallogr. D 57 (2001) 751.
[6] C. Slebodnik, J. Ibers, J. Biol. Inorg. Chem. 2 (1997) 521.
[7] T.G. Spiro, P.M. Kozlowski, Acc. Chem. Res. 34 (2001) 137.
[8] C. Rovira, J. Phys. -Condens. Matt. 15 (2002) 1809.
[9] E. Sigfridson, U. Ryde, J. Biol. Inorg. Chem. 4 (1999) 99.
[10] C. Rovira, B. Schulze, M. Eichinger, J.D. Evanseck, M. Parrinello, Biophys. J. 81 (2001) 435.
[11] J. Vojtechovsky, K. Chu, J. Berendzen, R.M. Sweet, I. Schlichting, Biophys. J. 77 (1999) 2153.
[12] S.-Y. Park, T. Yokoyama, N. Shibayama, Y. Shiro, J.R.H. Tame, J. Mol. Biol. 360 (2006) 690.
[13] S.E.V. Phillips, B.P. Schoenborn, Nature 292 (1981) 81.
[14] B. Shaanan, J. Mol. Biol. 171 (1983) 31.
[15] J.P. Collman, R.R. Gagne, C.A. Reed, T.R. Halbert, G. Lang, G.W.T. Robinson, J. Am. Chem. Soc. 97 (1975) 1427.
[16] G.B. Jameson, F.S. Molinaro, J.A. Ibers, J.P. Collman, J.I. Brauman, E. Rose, K.S. Suslick, J. Am. Chem. Soc. 102 (1980) 3224.
[17] F.A. Walker, J. Bowen, J. Am. Chem. Soc. 107 (1985) 7632.
[18] J.H. Bowen, N.V. Shokhirev, A.M. Raitsimring, D.H. Buttlaire, F.A. Walker, J. Phys. Chem. B 101 (1997) 8683.
[19] M. Ikeda-Saito, R.S. Lutz, D.A. Shelley, E.J. McKelvey, R. Mattera, H. Hori, J. Biol. Chem. 266 (1991) 23641.
[20] T.D. Smith, J.R. Pilbrow, Coord. Chem. Rev. 39 (1981) 295.
[21] D. Getz, E. Melamud, B.L. Silver, Z. Dori, J. Am. Chem. Soc. 97 (1975) 3846.
[22] E.A. Brucker, J.S. Olson, G.N. Phillips, Y. Dou, M. Ikeda-Saito, J. Biol. Chem. 271 (1996) 25419.
[23] I. Degtyarenko, R.M. Nieminen, C. Rovira, Biophys. J. 91 (2006) 2024.
[24] R. Czerminski, R. Elber, Prot. Func. Gen. 10 (1991) 70.
[25] J. Halpern, Science 227 (1985) 869.
[26] K.L. Brown, Chem. Rev. 105 (2005) 2075.
[27] L. Randaccio, S. Geremia, J. Wuerges, J. Organometal. Chem. 692 (2007) 1198.
[28] B. Kräutler, D. Arigoni, B.T. Golding (Eds.), Vitamin B12 and B12 proteins, Wiley–VCH, Weinheim, 1998.
[29] R. Banerjee, Chemistry and Biochemistry of B12, John Wiley and Sons, New York, 1999.
[30] L. Randaccio, S. Geremia, G. Nardin, J. Wuerges, Coord. Chem. Rev. 250 (2006) 1332.
[31] J. Halpern, D. Dolphin (Eds.), Chemistry and Significance of Vitamin B12 Model Systems, vol. 1, Wiley, NY, 1982, p. 501.
[32] S. Liccoccia, R. Paolesse, Struct. Bond. 84 (1995) 71.
[33] M.L. Ludwig, R.G. Mattews, Annu. Rev. Biochem. 66 (1997) 269.
[34] L. Randaccio, N. Bresciani-Pahor, E. Zangrando, L.G. Marzilli, Chem. Soc. Rev. 18 (1989) 225.
[35] L. Randaccio, Comments Inorg. Chem. 21 (1999) 327.
[36] C. Hu, U. Englert, Acta Crystallogr. E 57 (2001) m222.
[37] U. Englert, G. Heger, E. Kümmerle, R. Wang, Z. Kristallogr. 314 (1999) 71.
[38] G.J. Palenik, D.A. Sullivan, D.V. Naik, J. Am. Chem. Soc. 98 (1976) 1177.
[39] P.G. Jones, L. Yang, D. Steinborn, Acta Crystallogr. C 52 (1996) 2399.
[40] M. Semadeni, P.C. Chiu, M. Reinhard, Environ. Sci. Technol. 32 (1998) 1207.
[41] A.D. Follett, K.A. McNabb, A.A. Peterson, J.D. Scanlon, C.J. Cramer, K. McNeill, Inorg. Chem. 46 (2007) 1645–1654.
[42] D. Pratt, W.A. van der Donk, J. Am. Chem. Soc. 127 (2005) 384.
[43] CPMD program. Copyright IBM Corp. 1990–2003, Copyright MPI für Fesrkörperforschung, Stuttgart, Germany, 1997–2001.
[44] D. Marx, J. Hutter, in: J. Grotendorst (Ed.), Modern Methods and Algorithms of Quantum Chemistry, John von Neumann Institute for Computing, Julich, Germany, 2000, p. 301.
[45] R. Car, M. Parrinello, Phys. Rev. Lett. 55 (1985) 2471.
[46] M. Troullier, J.L. Martins, Phys. Rev. B 43 (1991) 1993.
[47] G. Louie, S. Froyen, M.L. Cohen, Phys. Rev. B 26 (1982) 1738.
[48] A.D. Becke, J. Chem. Phys. 84 (1986) 4524.
[49] J.P. Perdew, Phys. Rev. B 33 (1986) 8822.
[50] P. Ordejón, E. Artacho, J.M. Soler, Phys. Rev. B (Rapid Commun.) 53 (1996) R10441.
[51] J.M. Soler, E. Artacho, J.D. Gale, A. García, J. Junquera, P. Ordejón, D. Sánchez-Portal, J. Phys. -Condens. Matt. 14 (2002) 2745.
[52] J.P. Perdew, K. Burke, M. Ernzerhof, Phys. Rev. Lett. 77 (1996) 3865.
[53] P. Ordejón, Phys. Status Solidi B 217 (2000) 335.
[54] C. Rovira, M. Parrinello, Biophys. J. 78 (2000) 93.
[55] C. Rovira, K. Kunc, J. Hutter, P. Ballone, M. Parrinello, J. Phys. Chem A 101 (1997) 8914.
[56] K.M. Vogel, P.M. Kozlowski, M.Z. Zgierski, T.G. Spiro, J. Am. Chem. Soc. 121 (1999) 9915.
[57] R.H. Havlin, N. Godbout, R. Salzmann, M. Wojdelski, W. Arnold, C.E. Schulz, E. Oldfield, J. Am. Chem. Soc. 120 (1998) 3144.
[58] D.A. Scherlis, D.A. Estrin, Int. J. Quant. Chem. 87 (2002) 158.
[59] B.H. McMahon, B.P. Stojkovic, P.J. Hay, R.L. Martin, A.E. García, J. Chem. Phys. 113 (2000) 6831.

[60] J.N. Harvey, J. Am. Chem. Soc. 122 (2000) 12401.
[61] L.M. Blomberg, M.R.A. Blomberg, P.E.M. Siegbahn, J. Inorg. Biochem. 99 (2005) 949.
[62] D. Rutkowska-zbik, M. Witko, G. Stochel, J. Comput. Chem. 28 (2007) 825.
[63] C. Rovira, M. Parrinello, Chem. Eur. J. 5 (1999) 250.
[64] L.C. Dickinson, J.C.W. Chien, Proc. Natl. Acad. Sci. U.S.A. 77 (1980) 1235.
[65] M.Ø. Jensen, U. Röthlisberger, C. Rovira, Biophys. J. 89 (2005) 1744.
[66] B.M. Hoffman, D.H. Petering, Proc. Natl. Acad. Sci. U.S.A. 67 (1970) 627.
[67] D.A. Summerville, R.D. Jones, B.M. Hoffman, F. Basolo, J. Chem. Ed. 56 (1979) 157.
[68] B. Schulze, J.D. Evanseck, J. Am. Chem. Soc. 121 (1999) 6444.
[69] J. Ireta, J. Neugebauer, M. Scheffler, J. Phys. Chem. A 108 (2004) 5692.
[70] T. Kitagawa, M.R. Ondrias, D.L. Rousseau, M. Ikeda-Saito, T. Yonetani, Nature (1982) 869.
[71] J.A. Lukin, V. Simplaceanu, M. Zou, N.T. Ho, C. Ho, Proc. Natl. Acad. Sci. U.S.A. 97 (2000) 10354.
[72] H.C. Lee, M. Ikeda-Saito, T. Yonetani, R.S. Magliozzo, J. Peisach. Biochem. 31 (1992) 7274.
[73] L.M. Miller, M. Patel, M.R. Chance, J. Am. Chem. Soc. 118 (1996) 4511.
[74] G.B. Jameson, R.S. Drago, J. Am. Chem. Soc. 107 (1985) 3017.
[75] D.A. Scherlis, D.A. Estrin, J. Am. Chem. Soc. 123 (2001) 8436.
[76] T.G. Spiro, A.A. Jarzecki, Curr. Opin. Chem. Biol. 5 (2001) 715.
[77] J.P. Collman, Inorg. Chem. 36 (1997) 5145.
[78] G.B. Ray, X.-Y. Li, J.A. Ibers, J.L. Sessler, T.G. Spiro, J. Am. Chem. Soc. 116 (1994) 162.
[79] K. Spartalian, G. Lang, J.P. Collman, R.R. Gagne, C.A. Reed, J. Chem. Phys. 63 (1975) 5375.
[80] J. Mispelter, M. Momenteau, D. Lavalette, J.-M. Lhoste, J. Am. Chem. Soc. 105 (1983) 5165.
[81] E. Oldfield, H.C. Lee, C. Coretsopoulos, F. Adebodum, K.D. Park, S. Yang, J. Chung, B. Phillips, J. Am. Chem. Soc. 113 (1991) 8680.
[82] J.P. Collman, X. Zhang, K. Wong, J.I. Brauman, J. Am. Chem. Soc. 116 (1994) 6245.
[83] I.P. Gerothanassis, M. Momenteau, B. Loock, J. Am. Chem. Soc. 111 (1989) 7006.
[84] J.P. Collman, P.C. Herrmann, L. Fu, T.A. Eberspacher, M. Eubanks, B. Boitrel, P. Hayoz, X. Zhang, J.I. Brauman, V.W. Day, J. Am. Chem. Soc. 119 (1997) 3481.
[85] M. Momenteau, C.A. Reed, Chem. Rev. 94 (1994) 659.
[86] G.B. Jameson, G.A. Rodley, W.T. Robinson, R.R. Gagne, C.A. Reed, J.P. Collman, Inorg. Chem. 17 (1978) 850.
[87] K.P. Jensen, U. Ryde, J. Phys. Chem. A 107 (2003) 7539.
[88] N. Dölker, F. Maseras, P.E.M. Siegbahn, Chem. Phys. Lett. 386 (2004) 174.
[89] R.A. Kwiecien, I.V. Khavrutskii, D.G. Musaev, K. Morokuma, R. Banerjee, P. Paneth, J. Am. Chem. Soc. 128 (2006) 1287.
[90] C. Rovira, X. Biarnés, K. Kunc, Inorg. Chem. 43 (2004) 6628.
[91] C. Rovira, P.M. Kozlowski, J. Phys. Chem. B 111 (2007) 3251.
[92] T.G. Traylor, S. Vijay, Biochemistry 31 (1992) 2847.
[93] C. Mealli, M. Sabat, L. Marzilli, J. Am. Chem. Soc. 109 (1987) 1593.
[94] T.A. Stich, A.J. Brooks, N. Buan, T.C. Brunold, J. Am. Chem. Soc. 125 (2003) 5897.
[95] B.P. Hay, R.G. Finke, J. Am. Chem. Soc. 109 (1987) 8012.
[96] J. Seravalli, K.L. Brown, S.W. Ragsdale, J. Am. Chem. Soc. 123 (2001) 1786.
[97] G.N. Schrauzer, J.H. Grate, J. Am. Chem. Soc. 103 (1981) 541.
[98] T.-T. Tsou, M. Loots, J. Halpern, J. Am. Chem. Soc. 104 (1982) 623.
[99] M. Freindorf, P.M. Kozlowski, J. Am. Chem. Soc. 126 (2004) 1928.
[100] K.P. Jensen, U. Ryde, J. Am. Chem. Soc. 127 (2005) 9117.
[101] C. Rovira, K. Kunc, M. Parrinello, Inorg. Chem. 41 (2002) 4810.
[102] S. Miura, M.E. Tuckerman, M.J. Klein, J. Chem. Phys. 109 (1998) 5290.
[103] A. Ghosh, J. Biol. Inorg. Chem. 11 (2006) 712.
[104] W. Clegg, R.J. Anderson, B.T. Golding, Acta Crystallogr. C 45 (1989) 383.
[105] L. Randaccio, M. Furlan, S. Geremia, M. Slouf, I. Srnova, Inorg. Chem. 39 (2000) 3403.
[106] L. Ouyang, P. Rulis, W.Y. Ching, G. Nardin, L. Randaccio, Inorg. Chem. 43 (2004) 1235.